

Tuning the Electrochemical Performance of Titanium Carbide MXene by Controllable In Situ Anodic Oxidation

Jun Tang, Tyler S. Mathis, Narendra Kurra, Asia Sarycheva, Xu Xiao, Mohamed N. Hedhili, Qiu Jiang, Husam N. Alshareef, Baomin Xu, Feng Pan, and Yury Gogotsi*

Abstract: MXenes are a class of two-dimensional (2D) transition metal carbides, nitrides and carbonitrides that have shown promise for high-rate pseudocapacitive energy storage. However, the effects that irreversible oxidation have on the surface chemistry and electrochemical properties of MXenes are still not understood. Here we report on a controlled anodic oxidation method which improves the rate performance of titanium carbide MXene ($\text{Ti}_3\text{C}_2\text{T}_x$, T_x refers to $-\text{F}$, $=\text{O}$, $-\text{Cl}$ and $-\text{OH}$) electrodes in acidic electrolytes. The capacitance retention at 2000 mVs^{-1} (with respect to the lowest scan rate of 5 mVs^{-1}) increases gradually from 38 % to 66 % by tuning the degree of anodic oxidation. At the same time, a loss in the redox behavior of $\text{Ti}_3\text{C}_2\text{T}_x$ is evident at high anodic potentials after oxidation. Several analysis methods are employed to reveal changes in the structure and surface chemistry while simultaneously introducing defects, without compromising electrochemically active sites, are key factors for improving the rate performance of $\text{Ti}_3\text{C}_2\text{T}_x$. This study demonstrates improvement of the electrochemical performance of MXene electrodes by performing a controlled anodic oxidation.

Introduction

MXenes are a quickly growing class of two-dimensional (2D) nanomaterials comprised of transition metal carbides, nitrides, and carbonitrides, which exhibit a unique combination of hydrophilicity and metallic electrical conductivity.^[1–11] MXenes are typically synthesized by top-down wet chemical method through selective etching of A atoms from ternary layered MAX phases, where M stands for an early transition metal (Ti, Nb, Mo, V, Cr, Ta, etc), A is an element from Group 13 or 14 (Al, Si, Ga, or In), and X is carbon and/or nitrogen.^[12] The resulting MXenes can be described by the general formula $\text{M}_{n+1}\text{X}_n\text{T}_x$ ($n = 1, 2, 3$), and T_x represents the surface

functional groups such as $-\text{F}$, $=\text{O}$, $-\text{Cl}$ and $-\text{OH}$. Their compositional versatility, variable transition metal redox chemistry, tunable interlayer spacing, and controllable surface chemistry, make MXenes suitable for a wide range of applications from electromagnetic shielding to energy storage.^[13,14] MXenes exhibit intercalation pseudocapacitance where redox reactions take place with ultrafast ion kinetics, which is distinctly different from both, the sluggish ion diffusion in bulk battery electrodes and the formation of electrical double layers (EDL) at the surfaces of porous carbon electrodes.^[15,16] The ability of MXenes to rapidly intercalate a variety of cations is key for developing high rate electrodes for hybrid metal-ion capacitors and multi-valent ion batteries.^[16–22]

Titanium carbide ($\text{Ti}_3\text{C}_2\text{T}_x$), the first reported and the best studied MXene, has the highest reported electronic conductivity ($> 10000 \text{ Scm}^{-1}$) among all MXenes,^[23] good packing density (up to 4 g cm^{-3}), and proton induced pseudocapacitance, which results in high volumetric capacitance, upwards of 1500 F cm^{-3} with high rate performance in relatively thin films.^[14] The 2D morphology, surface functionality, intercalated water molecules, redox active transition metal oxide-like surfaces, and high electronic conductivity are the key factors for the high rate pseudocapacitive behavior of MXenes.^[24] It was reported that the origin of the pseudocapacitance of MXenes is mainly due to $=\text{O}$ surface functional groups.^[25] However, the restacking of MXene sheets when they are reassembled into free-standing films impedes ion transport, limiting the overall rate performance.^[3,14] This restacking issue was circumvented through vertical alignment of liquid crystalline MXene electrodes, in which thickness independent capacitive behavior was demonstrated for industrial scale thicknesses ($\approx 200 \mu\text{m}$).^[3] Furthermore, methods using spacers such as carbon materials, polymers, and

[*] J. Tang, T. Mathis, Dr. N. Kurra, A. Sarycheva, Dr. X. Xiao, Prof. Y. Gogotsi

A.J. Drexel Nanomaterials Institute and Department of Materials Science and Engineering, Drexel University
Philadelphia, PA 19104 (USA)
E-mail: gogotsi@drexel.edu

J. Tang, Prof. B. Xu
Department of Materials Science and Engineering, Southern University of Science and Technology
Shenzhen, Guangdong Province 518055 (P. R. China)

J. Tang, Prof. F. Pan
School of Advanced Materials, Peking University Shenzhen Graduate School, Peking University
Shenzhen, Guangdong Province 518055 (P. R. China)

Dr. M. N. Hedhili
King Abdullah University of Science and Technology (KAUST)
Core Labs, Thuwal, 23955-6900 (Saudi Arabia)

Dr. Q. Jiang, Prof. H. N. Alshareef
Materials Science and Engineering, Physical Science and Engineering Division, King Abdullah University of Science and Technology (KAUST), Thuwal 23955-6900 (Saudi Arabia)

Supporting information and the ORCID identification number(s) for the author(s) of this article can be found under <https://doi.org/10.1002/anie.201911604>.

surfactants, or by the introduction of holes into the MXene sheets by chemical etching, were also used to improve electrochemical performance.^[22,26,27] However, these improvements were achieved at the expense of volumetric performance. There are no systematic studies on the influence of surface chemistry on the intrinsic electrochemical performance of titanium carbide electrodes. Previous work has shown that irreversible oxidation of $\text{Ti}_3\text{C}_2\text{T}_x$ can increase the interlayer spacing, but this resulted in low capacitance due to the formation of titania and loss of electrochemically active titanium sites.^[28]

Herein, a new and simple approach of in situ anodic oxidation has been developed for improving the rate performance of restacked MXene electrodes. This controllable oxidation process slightly enlarges the interlayer spacing and introduces holes into the MXene structure, without damaging the electrochemical active sites, improving the rate performance of $\text{Ti}_3\text{C}_2\text{T}_x$. This finding may help in the design of advanced high-rate MXene based energy storage devices, such as microsupercapacitors, energy storing textiles and electrochromic or energy-storing windows.

Results and Discussion

$\text{Ti}_3\text{C}_2\text{T}_x$ MXene operates at cathodic potentials and exhibits a pair of broad oxidation and reduction peaks in acidic electrolytes.^[14] The typical potential window for cycling $\text{Ti}_3\text{C}_2\text{T}_x$ MXene is negative (−1.2 V to −0.2 V vs. $\text{Hg}/\text{Hg}_2\text{SO}_4$).^[13] The redox nature is attributed to the protonation/deprotonation of surface functional groups with concomitant changes of Ti redox state.^[29] However, at anodic potentials (>0 V vs. $\text{Hg}/\text{Hg}_2\text{SO}_4$), $\text{Ti}_3\text{C}_2\text{T}_x$ is prone to irreversible oxidation, as shown in Figure 1a. The reversible oxidation peak current (at a potential of −0.8 V vs. $\text{Hg}/\text{Hg}_2\text{SO}_4$) is only 14% of the magnitude of the current of the irreversible oxidation peak (at ≈0.4 V vs. $\text{Hg}/\text{Hg}_2\text{SO}_4$). Following irreversible anodic oxidation, $\text{Ti}_3\text{C}_2\text{T}_x$ becomes electrochemically inactive as evident from the decrease in the cyclic voltammetry (CV) area (losing >50% of its initial capacitance) during cathodic potential window of operation (Figure 1b). This permanent change in the electrochemical behavior of $\text{Ti}_3\text{C}_2\text{T}_x$ is likely due to changes in the structure of $\text{Ti}_3\text{C}_2\text{T}_x$ beyond the modification of the surface composition.

To investigate the structural changes occurring due to irreversible oxidation, X-ray diffraction (XRD) patterns of $\text{Ti}_3\text{C}_2\text{T}_x$ electrodes before and after oxidation are shown in Figure 1c. Interestingly, the (002) peak is downshifted, with a higher *d*-spacing of 1.5 nm, when compared to the (002) peak of pristine $\text{Ti}_3\text{C}_2\text{T}_x$, which has a typical *d*-spacing of 1.2 nm. Irreversible oxidation caused expansion of the titanium carbide lattice by changing the surface composition of $\text{Ti}_3\text{C}_2\text{T}_x$. By comparing the Raman spectra of pristine and anodically oxidized $\text{Ti}_3\text{C}_2\text{T}_x$, it is evident that the relative intensities of the MXene peaks at 205 and 723 cm^{-1} decrease and almost disappear (Figure 1d). The peaks at these two positions are assigned to out-of-plane vibrations of Ti, C, and O atoms and C atoms of $\text{Ti}_3\text{C}_2\text{T}_x$, respectively, corresponding to the active =O sites which contributes to the pseudocapac-

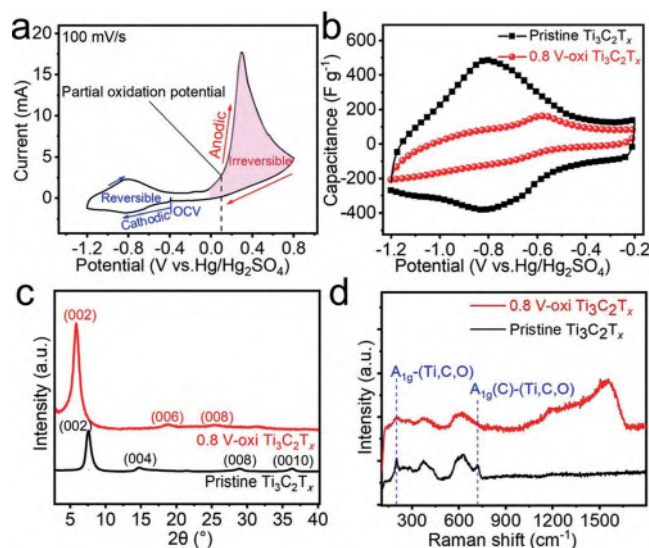
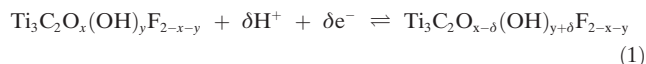


Figure 1. Reversible and irreversible electrochemical behavior of $\text{Ti}_3\text{C}_2\text{T}_x$. a) Cyclic voltammogram (CV) of $\text{Ti}_3\text{C}_2\text{T}_x$ with a potential range beyond the stable operating potential of $\text{Ti}_3\text{C}_2\text{T}_x$ at a scan rate of 100 mV s^{-1} . b) Comparison of CVs of $\text{Ti}_3\text{C}_2\text{T}_x$ in the standard potential window for pristine MXene and after anodic oxidation at 0.8 V (0.8 V-oxi). Ex situ c) XRD patterns and d) Raman spectra of pristine $\text{Ti}_3\text{C}_2\text{T}_x$ and $\text{Ti}_3\text{C}_2\text{T}_x$ anodically oxidized at 0.8 V vs. $\text{Hg}/\text{Hg}_2\text{SO}_4$.

citance of $\text{Ti}_3\text{C}_2\text{T}_x$, according to the following reversible redox reaction:^[25]



The decreased intensity of the peaks at 205 cm^{-1} and 723 cm^{-1} may be affected by the nearby defects and holes resulting that the out-of-plane vibrations became very weak. A broad peak is also observed in the range of 1100 to 1600 cm^{-1} following irreversible oxidation. This could be attributed to C–C bonds from amorphous carbon produced by the oxidation of $\text{Ti}_3\text{C}_2\text{T}_x$,^[30–32] which has been verified by the X-ray photoelectron spectroscopy (XPS) results showing a large amount of sp^3 bonding. This peak can also be due to the dissolution of oxidized titanium in the acidic electrolyte, which possibly exposes carbon atoms on the surface of $\text{Ti}_3\text{C}_2\text{T}_x$.

In order to study the effect of oxidation at low anodic potentials, cycling to 0.1 V vs. $\text{Hg}/\text{Hg}_2\text{SO}_4$ was chosen as the potential for partial oxidation (Figure 1a, dashed line). For controlling the extent of oxidation, multiple CV sweeps were performed. The corresponding CV profiles at 100 mV s^{-1} are shown in Figure 2a and no significant changes can be observed. With an increase in the number of oxidation cycles, the reversible redox peaks gradually shift toward lower potentials and the peak current density increases slightly. The capacitive current density in the potential range of −0.4 to 0 V vs. $\text{Hg}/\text{Hg}_2\text{SO}_4$ also increases after the first sweep to 0.1 V vs. $\text{Hg}/\text{Hg}_2\text{SO}_4$ and remains almost constant during further cycles of partial oxidation. The current density in this potential range (−0.4 to 0 V vs. $\text{Hg}/\text{Hg}_2\text{SO}_4$) is mainly contributed by EDL capacitance, which is governed by the accessible surface

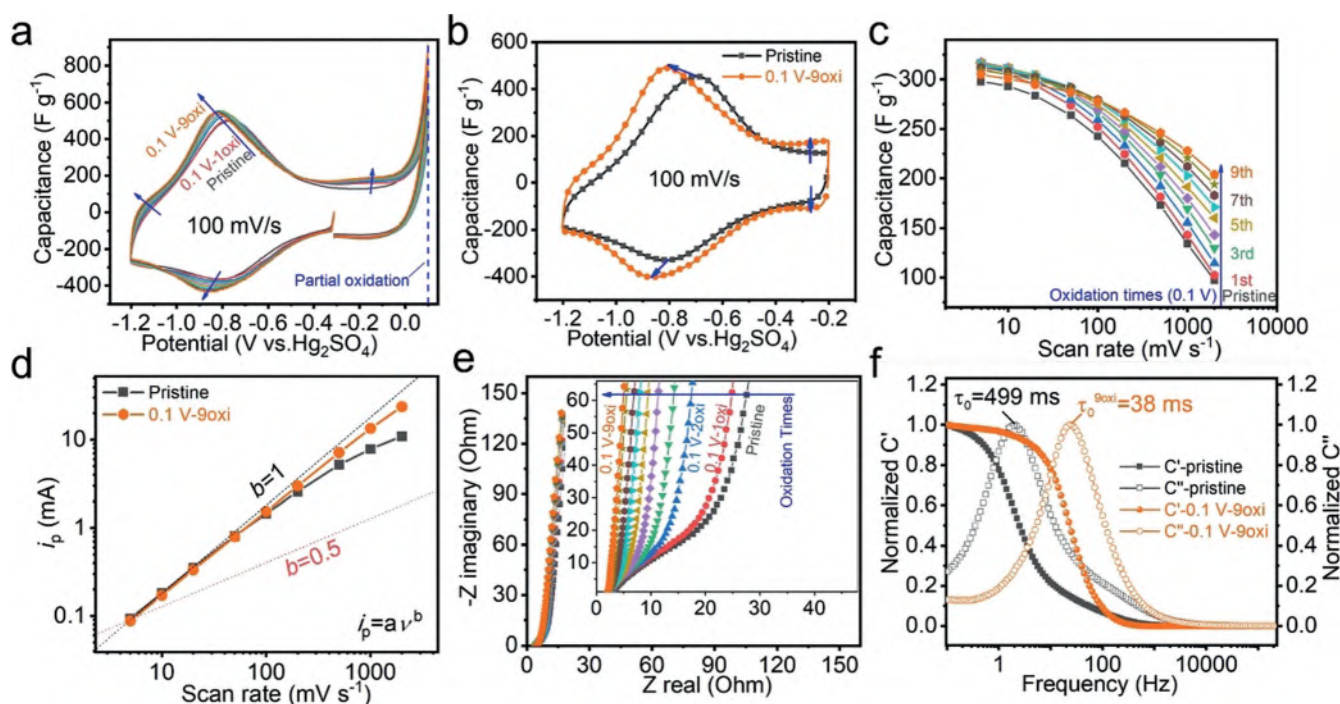


Figure 2. Controlling the rate performance of titanium carbide MXene through anodic oxidation. CV profiles of $\text{Ti}_3\text{C}_2\text{T}_x$ a) partially oxidized in 1 M H_2SO_4 for nine cycles and b) in the stable potential window before and after 9 cycles of partial oxidation (0.1 V-9oxi). c) Capacitance vs. scan rate. d) Plots of b values for pristine and 9-cycles oxidized $\text{Ti}_3\text{C}_2\text{T}_x$. e) EIS spectra of $\text{Ti}_3\text{C}_2\text{T}_x$ MXene after cycle of partial anodic oxidation. f) Normalized real (C') and imaginary (C'') parts of capacitance versus frequency.

area. Accordingly, the current density changes in this potential range imply that the interlayer space of $\text{Ti}_3\text{C}_2\text{T}_x$ is enlarged by a single CV sweep of partial oxidation and cannot be increased further with more cycles at the same potential. Similar results are obtained for the CVs in a negative potential window (−1.2 to −0.2 V vs. $\text{Hg}/\text{Hg}_2\text{SO}_4$) after partial oxidation, as displayed in Figure 2b. The increased current density for both the redox potential range (−1.2 V to −0.4 V vs. $\text{Hg}/\text{Hg}_2\text{SO}_4$) and EDL response region (−0.4 V to −0.2 V vs. $\text{Hg}/\text{Hg}_2\text{SO}_4$), indicates improved charge storage. Even though the capacitance at low scan rates does not change much, the effect of partial oxidation is strongly pronounced at high scan rates. CVs for different scan rates are also shown in Figure S2 (Supporting Information) for comparison between the pristine and 9-cycles partially oxidized $\text{Ti}_3\text{C}_2\text{T}_x$ (0.1 V-9oxi). The advantage of 0.1 V-9oxi $\text{Ti}_3\text{C}_2\text{T}_x$ over pristine $\text{Ti}_3\text{C}_2\text{T}_x$ at higher scan rates indicates that partial oxidation increases the rate performance but not the intrinsic capacitance of $\text{Ti}_3\text{C}_2\text{T}_x$.

As a result, as shown in Figure 2c, the capacitance at 2000 mV s^{-1} increases significantly, as $\text{Ti}_3\text{C}_2\text{T}_x$ is successively partially oxidized. The capacitance retention for 0.1 V-9oxi $\text{Ti}_3\text{C}_2\text{T}_x$ at 2000 mV s^{-1} compared to that at 5 mV s^{-1} is 66 %, which is almost two times higher than the capacitance retention of pristine $\text{Ti}_3\text{C}_2\text{T}_x$. It should be noted that the capacitance of $\text{Ti}_3\text{C}_2\text{T}_x$ at lower scan rates ($< 20 \text{ mV s}^{-1}$) increases during the initial 5 cycles of partial oxidation but then decreases slightly when oxidized more than 5 cycles, as shown in Figure S3 (Supporting Information). The capacitance of 0.1 V-9oxi $\text{Ti}_3\text{C}_2\text{T}_x$ at 5 mV s^{-1} decreases to nearly the

same value as the pristine electrode, but then remains almost the same as the 0.1 V-8oxi $\text{Ti}_3\text{C}_2\text{T}_x$ electrode as the scan rate increases to 2000 mV s^{-1} . In 3 M H_2SO_4 electrolyte, the effect of anodic oxidation on the electrochemical performance of $\text{Ti}_3\text{C}_2\text{T}_x$ was also investigated and the same rate performance improvement was observed (Figure S4, Supporting Information). The oxidized $\text{Ti}_3\text{C}_2\text{T}_x$ also showed excellent cycling performance with only a slight decrease in capacitance after 10000 cycles (Figure S13, Supporting Information). Anodic oxidation at different potentials can also be used to control the degree of oxidation (Figure S5, Supporting Information). Similar improvements in rate performance were observed for anodic oxidation performed below 0.3 V vs. $\text{Hg}/\text{Hg}_2\text{SO}_4$. When only one cycle of oxidation is performed, the best rate performance is obtained at 0.3 V, with 51 % retention at 2000 mV s^{-1} of the initial capacitance at 5 mV s^{-1} . When the potential goes above 0.3 V, the capacitance decreases rapidly, likely due to complete oxidation of surface layer of $\text{Ti}_3\text{C}_2\text{T}_x$ and the formation of TiO_2 . This result shows again that the rate performance can be tuned by controlling the degree of oxidation without decreasing the capacitance. To analyze the difference in charge storage kinetics between pristine and partially oxidized $\text{Ti}_3\text{C}_2\text{T}_x$, the relationship between the peak current and the scan rate are shown in Figure 2d. By using the Equation (2)

$$i_p = av^b, \quad (2)$$

where v is the scan rate and i_p is the peak current at different scan rates, and a and b are variables, the kinetic performance

of the electrodes can be compared conveniently as the b -value is indicative of the charge storage kinetics. Surface controlled charge storage processes have a characteristic b value of 1, while diffusion-limited processes give b values of 0.5.^[33] For the pristine $\text{Ti}_3\text{C}_2\text{T}_x$ film, the b value deviates from 1 when the scan rate is higher than 200 mV s^{-1} . However, after 9 cycles of partial oxidation, the b value is still near 1 up to scan rates of 2000 mV s^{-1} , further proving that partial oxidation improves the performance of $\text{Ti}_3\text{C}_2\text{T}_x$ at high rates by improving accessibility to the MXene surface and minimizing diffusion limitations. Electrochemical impedance spectra (EIS) of partially oxidized $\text{Ti}_3\text{C}_2\text{T}_x$ electrodes shown in Figure 2e are consistent with the rate performance data. The impedance of $\text{Ti}_3\text{C}_2\text{T}_x$ in the medium frequency regime decreases gradually with partial oxidation cycle number, matching the gradually increasing rate performance. The decreased impedance in this frequency range corresponds to reduction in ion diffusion limitations, which contributes to the final rate performance. The improved electrochemical kinetics of the partially oxidized electrodes is further supported by their small relaxation time constants, τ_0 (the minimum time needed to discharge all energy stored with an efficiency greater than 50%).^[34] As shown in Figure 2f, τ_0 is around 500 ms for pristine $\text{Ti}_3\text{C}_2\text{T}_x$ and $\tau_0^{9\text{oxi}}$ is 38 ms, indicating that charge response of 0.1V-9oxi $\text{Ti}_3\text{C}_2\text{T}_x$ is almost 13 times faster than pristine. The improvement in rate performance was also observed in KOH and Li_2SO_4 electrolytes, indicating that controlled anodic oxidation is universally applicable for improving the rate performance of $\text{Ti}_3\text{C}_2\text{T}_x$ in various electrolytes.

To understand the mechanism behind the rate performance improvements after partial oxidation, ex situ XRD experiments and in situ electrochemical Raman experiments were performed on the pristine $\text{Ti}_3\text{C}_2\text{T}_x$ and the oxidized $\text{Ti}_3\text{C}_2\text{T}_x$ electrodes (Figure 3a and Figure 3d). The interlayer space can be increased at relatively low potential (0.1 V) and does not change noticeably until the potential increased to a higher value of 0.9 V (Figure 3b). The (002) peak of oxidized $\text{Ti}_3\text{C}_2\text{T}_x$ shifts toward smaller degrees, indicating increased interlayer space. For pristine $\text{Ti}_3\text{C}_2\text{T}_x$, the interlayer distance is 1.2 nm, which then increases to 1.4 nm by partial oxidation at 0.1 V. Oxidation at 0.9 V only increases the interlayer space by another 0.1 nm. Such kind of changes in the interlayer space is highly consistent with the current density changes in the double-layer capacitance region, as discussed in Figure 2a. High-potential oxidation results in dramatic changes to the surface chemistry as shown in Figure 3d. The peaks assigned to $\text{Ti}_3\text{C}_2\text{T}_x$ functional groups (205 cm^{-1} and 723 cm^{-1}) decrease significantly when the potential goes past 0.5 V and the G band of carbon appears (1580 cm^{-1} , Figure S7, Supporting Information). The absence of out-of-plane peaks and therefore structural changes result in the dramatic capacitance fading for higher potential oxidation as shown in Figure 1b and Figure S5 (Supporting Information). In conclusion, oxidation at a safe potential of 0.1 V increases the interlayer spacing of $\text{Ti}_3\text{C}_2\text{T}_x$ while avoiding irreversible loss of electrochemically active surface of 2D $\text{Ti}_3\text{C}_2\text{T}_x$ nanosheets. As a result, improved high rate electrochemical performance is obtained without noticeable

capacitance losses or even some improvement at low rates. Moreover, as shown in the TEM images in Figure 3b and c, the 2D $\text{Ti}_3\text{C}_2\text{T}_x$ sheets became porous following oxidation at 0.1 V for 9 cycles. Even more pores are visible when the electrode is oxidized at 0.9 V (Figure S1, Supporting Information). From optic images, we also observed a clear morphology change of the $\text{Ti}_3\text{C}_2\text{T}_x$ film from a smooth to a rough surface at 0.9 V (Figure S6, Supporting Information).

XPS investigations were performed to characterize the surface composition of the electrodes before and after oxidation and to determine if there were changes in the oxidation state of titanium. High resolution XPS spectra of Ti 2p and C 1s core levels from ($\text{Ti}_3\text{C}_2\text{T}_x$) samples (pristine, 0.1 V-9oxi, and 0.9 V-oxi) are shown in Figure 3e. We can clearly observe an increase of the contribution of components related to TiO_2 and $\text{TiO}_{2-x}\text{F}_x$ to the Ti 2p core level spectrum following anodic oxidation. Furthermore, we have observed a decrease of the contribution of Ti-C bonds relative to the contribution of C-C, C-O, and C=O bonds to the C 1s core level spectrum following electrochemical oxidation. In summary, during the oxidation process, C-Ti bonds are gradually broken and C-C and $\text{TiO}_{2-x}\text{F}_x$ species are formed.

Based on the in situ Raman, TEM, ex situ XRD, and XPS results, a possible mechanism of the micro-structure changes occurring during oxidation is schematically illustrated in Figure 3f. First, part of the surface Ti atoms connected to =O moieties are removed during the anodic de-functionalization process forming $\text{TiO}_{2-x}\text{F}_x$, according to the XPS results. Several C atoms are then exposed at the surface so that the original Ti-C-Ti structure at the surface produces C atoms which likely bond with adjacent exposed C atoms with free electrons, forming a C-C bond (most likely in the form of amorphous carbon according to the XPS and Raman results). Continued oxidation and formation of TiO_2 could result in disruption of the MXene sheets and significant capacitance losses. The pin holes observed in the SEM and TEM images are also likely being formed during this process (Figure S1, Supporting Information).

In summary, controlled anodic oxidation increases the interlayer space of $\text{Ti}_3\text{C}_2\text{T}_x$ and gradually creates pores in the 2D nanosheets without significantly depleting the electrochemically active oxygen functional groups on the surface of $\text{Ti}_3\text{C}_2\text{T}_x$, resulting in porous $\text{Ti}_3\text{C}_2\text{T}_x$ electrodes with improved ion transport. The improved high-rate charge storage capability of partially oxidized $\text{Ti}_3\text{C}_2\text{T}_x$ electrodes enables simultaneous high-power and high energy performance across a wider range of power densities, as shown in Figure 4. Though it is not advisable to calculate energy and power densities for 3-electrode cells, comparison of these performance metrics here is useful and fair since we are only comparing the energy and power densities of the electrodes from this study. All the electrodes exhibit a maximum specific energy density of $\approx 40 \text{ Wh kg}^{-1}$ at a power density of $\approx 750 \text{ W kg}^{-1}$. The energy density delivered by pristine $\text{Ti}_3\text{C}_2\text{T}_x$ is only 15 Wh kg^{-1} at a power density of 130 kW kg^{-1} , while the 0.1 V-9oxi $\text{Ti}_3\text{C}_2\text{T}_x$ delivers a much higher energy density of 27 Wh kg^{-1} at a higher power density of 193 kW kg^{-1} . As shown in Figure 4b, there is an improvement in the high power performance of $\text{Ti}_3\text{C}_2\text{T}_x$ partially oxidized at

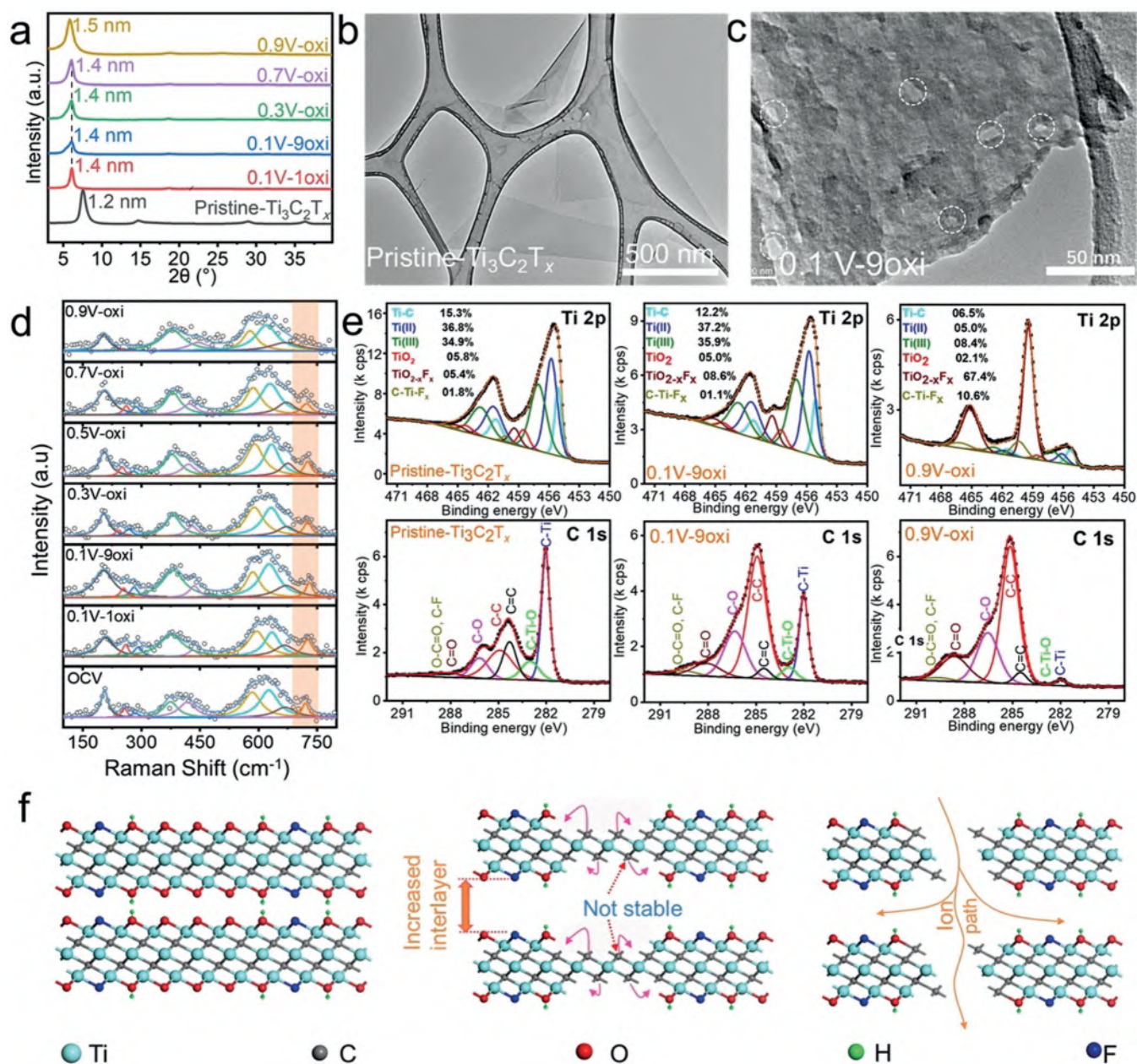


Figure 3. Understanding the mechanism of rate performance improvement of MXene electrodes. a) XRD patterns of $\text{Ti}_3\text{C}_2\text{T}_x$ electrodes oxidized at different potentials. TEM images of b) pristine and c) 0.1 V-9oxi $\text{Ti}_3\text{C}_2\text{T}_x$ MXene. d) In situ electrochemical Raman spectra of $\text{Ti}_3\text{C}_2\text{T}_x$ electrodes at different anodic potentials. e) Core level Ti(2p), C(1s) spectra for pristine, 0.1 V-9oxi and 0.9 V-oxi $\text{Ti}_3\text{C}_2\text{T}_x$ electrodes. f) Schematic illustration of the anodic oxidation process.

relatively low potentials (0.1 V and 0.3 V vs. $\text{Hg}/\text{Hg}_2\text{SO}_4$). However, when the oxidation potential is extended beyond 0.3 V, both the energy and power densities decrease rapidly, indicating excessive oxidation of MXene. Based on the improvements in the electrochemical performance of the partially oxidized $\text{Ti}_3\text{C}_2\text{T}_x$ at high rates, this simple anodic oxidation can be used as pre-treatment (conditioning) to improve MXene-based supercapacitors.

Conclusion

The electrochemical performance of $\text{Ti}_3\text{C}_2\text{T}_x$ MXene was improved through a controlled electrochemical oxidation process. Repeated cycling of $\text{Ti}_3\text{C}_2\text{T}_x$ electrodes to anodic potentials slightly beyond their typical operational window increases the interlayer spacing between the 2D nanosheets and introduces pores into the MXene layers without damaging the electrochemically active sites. This optimized partial oxidation process can double the capacitance retention of

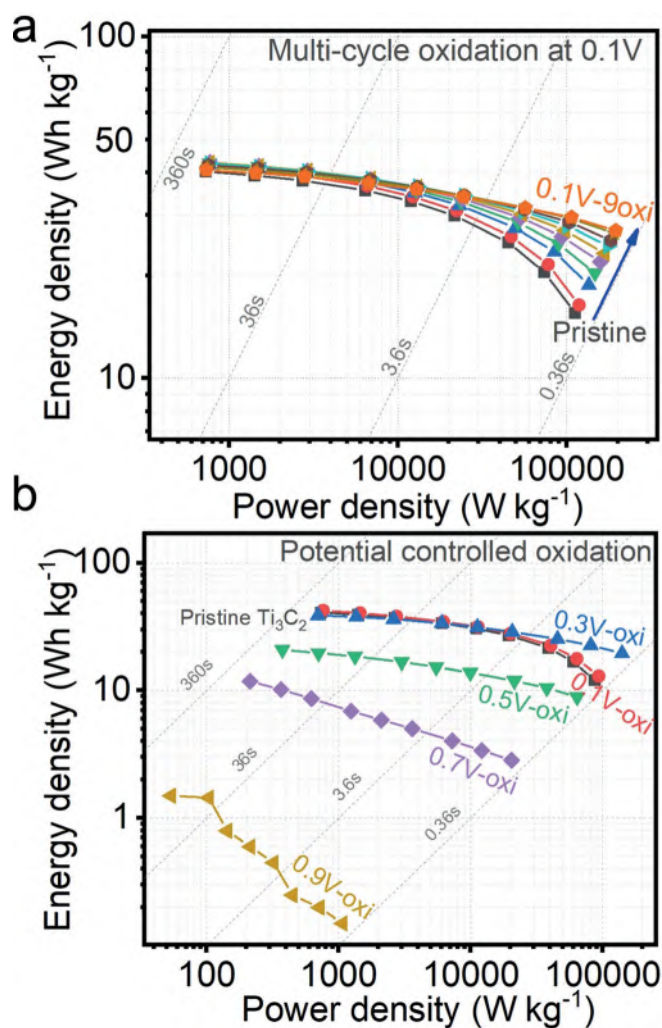


Figure 4. Specific energy vs. power density plots of $\text{Ti}_3\text{C}_2\text{T}_x$ MXene electrodes with varying degrees of anodic oxidation. Ragone plots of $\text{Ti}_3\text{C}_2\text{T}_x$ MXene electrodes after a) repeated oxidation cycles at 0.1 V (vs. $\text{Hg}/\text{Hg}_2\text{SO}_4$) and b) after a single oxidation cycle at different potentials (vs. $\text{Hg}/\text{Hg}_2\text{SO}_4$).

$\text{Ti}_3\text{C}_2\text{T}_x$ in acidic electrolytes at high-rates. Partially oxidized $\text{Ti}_3\text{C}_2\text{T}_x$ electrodes exhibited $\approx 30\%$ improved kinetics and hence improved rate performance over pristine MXene electrodes.

Acknowledgements

We thank Chuanfang (John) Zhang for the help with material synthesis and Christine Hatter for the help with FTIR analysis. J.T. was sponsored by the China Scholarship Council (CSC). Research on electrochemical interfaces at Drexel University was supported by the Fluid Interface Reactions, Structures, and Transport (FIRST) Center, an Energy Frontier Research Center (EFRC) funded by the U.S. Department of Energy, Office of Science, and Office of Basic Energy Sciences. Collaboration between King Abdullah University of Science and Technology (KAUST) and Drexel University was supported by KAUST–Drexel Competitive Research Grant

(URF/1/ 2963-01-01). Collaboration between Southern University of Science and Technology (SUSTech) and Drexel University was supported by the Fundamental Research (Discipline Arrangement) Project funding from Shenzhen Science and Technology Innovation Committee (Grant No. JCYJ20170412154554048), the Peacock Team Project funding from Shenzhen Science and Technology Innovation Committee (Grant No. KQTD2015033110182370).

Conflict of interest

The authors declare no conflict of interest.

Keywords: anodic oxidation · high-rate energy storage · MXenes · pseudocapacitance · surface chemistry

How to cite: *Angew. Chem. Int. Ed.* **2019**, *58*, 17849–17855
Angew. Chem. **2019**, *131*, 18013–18019

- [1] B. Anasori, M. R. Lukatskaya, Y. Gogotsi, *Nat. Rev. Mater.* **2017**, *2*, 16098.
- [2] F. Shahzad, M. Alhabeib, C. B. Hatter, B. Anasori, S. M. Hong, C. M. Koo, Y. Gogotsi, *Science* **2016**, *353*, 1137–1140.
- [3] Y. Xia, T. S. Mathis, M.-Q. Zhao, B. Anasori, A. Dang, Z. Zhou, H. Cho, Y. Gogotsi, S. Yang, *Nature* **2018**, *557*, 409.
- [4] Y. Gogotsi, B. Anasori, *ACS Nano* **2019**, *13*, 8491–8494.
- [5] A. VahidMohammadi, M. Mojtavavi, N. M. Caffrey, M. Wanunu, M. Beidaghi, *Adv. Mater.* **2019**, *31*, 1970057.
- [6] K. Kim, Y. Ando, A. Sugahara, S. Ko, Y. Yamada, M. Otani, M. Okubo, A. Yamada, *Chem. Mater.* **2019**, *31*, 5190–5196.
- [7] W. Tian, A. VahidMohammadi, Z. Wang, L. Ouyang, M. Beidaghi, M. M. Hamed, *Nat. Commun.* **2019**, *10*, 2558.
- [8] H.-C. Fu, V. Ramalingam, H. Kim, C.-H. Lin, X. Fang, H. N. Alshareef, J.-H. He, *Adv. Energy Mater.* **2019**, *9*, 1900180.
- [9] Q. Jiang, N. Kurra, K. Maleski, Y. Lei, H. Liang, Y. Zhang, Y. Gogotsi, H. N. Alshareef, *Adv. Energy Mater.* **2019**, *9*, 1901061.
- [10] T. Ling, P. Da, X. Zheng, B. Ge, Z. Hu, M. Wu, X.-W. Du, W.-B. Hu, M. Jaroniec, S.-Z. Qiao, *Sci. Adv.* **2018**, *4*, eaau6261.
- [11] J. Ran, G. Gao, F.-T. Li, T.-Y. Ma, A. Du, S.-Z. Qiao, *Nat. Commun.* **2017**, *8*, 1–10.
- [12] M. W. Barsoum, *MAX Phases: Properties of Machinable Ternary Carbides and Nitrides*, Wiley, Hoboken, **2013**.
- [13] M. R. Lukatskaya, O. Mashtalir, C. E. Ren, Y. Dall'Agnese, P. Rozier, P. L. Taberna, M. Naguib, P. Simon, M. W. Barsoum, Y. Gogotsi, *Science* **2013**, *341*, 1502–1505.
- [14] M. R. Lukatskaya, S. Kota, Z. Lin, M.-Q. Zhao, N. Shpigel, M. D. Levi, J. Halim, P.-L. Taberna, M. W. Barsoum, P. Simon, et al., *Nat. Energy* **2017**, *2*, 17105.
- [15] M. Okubo, A. Sugahara, S. Kajiyama, A. Yamada, *Acc. Chem. Res.* **2018**, *51*, 591–599.
- [16] A. VahidMohammadi, A. Hadjikhani, S. Shahbazmohamadi, M. Beidaghi, *ACS Nano* **2017**, *11*, 11135–11144.
- [17] H. Liang, Z. Cao, F. Ming, W. Zhang, D. H. Anjum, Y. Cui, L. Cavallo, H. N. Alshareef, *Nano Lett.* **2019**, *19*, 3199–3206.
- [18] M. Naguib, J. Halim, J. Lu, K. M. Cook, L. Hultman, Y. Gogotsi, M. W. Barsoum, *J. Am. Chem. Soc.* **2013**, *135*, 15966–15969.
- [19] F. Ming, H. Liang, W. Zhang, J. Ming, Y. Lei, A.-H. Emwas, H. N. Alshareef, *Nano Energy* **2019**, *62*, 853–860.
- [20] X. Wang, S. Kajiyama, H. Iinuma, E. Hosono, S. Oro, I. Moriguchi, M. Okubo, A. Yamada, *Nat. Commun.* **2015**, *6*, 6544.

- [21] M. Naguib, J. Come, B. Dyatkin, V. Presser, P.-L. Taberna, P. Simon, M. W. Barsoum, Y. Gogotsi, *Electrochem. Commun.* **2012**, *16*, 61–64.
- [22] Z. Ling, C. E. Ren, M.-Q. Zhao, J. Yang, J. M. Giammarco, J. Qiu, M. W. Barsoum, Y. Gogotsi, *Proc. Natl. Acad. Sci. USA* **2014**, *111*, 16676–16681.
- [23] *2D Metal Carbides and Nitrides (MXenes): Structure, Properties and Applications* (Eds.: B. Anasori, Y. Gogotsi), Springer International Publishing, Berlin, **2019**.
- [24] N. Shpigel, M. D. Levi, S. Sigalov, T. S. Mathis, Y. Gogotsi, D. Aurbach, *J. Am. Chem. Soc.* **2018**, *140*, 8910–8917.
- [25] M. Hu, Z. Li, T. Hu, S. Zhu, C. Zhang, X. Wang, *ACS Nano* **2016**, *10*, 11344–11350.
- [26] J. Luo, W. Zhang, H. Yuan, C. Jin, L. Zhang, H. Huang, C. Liang, Y. Xia, J. Zhang, Y. Gan, et al., *ACS Nano* **2017**, *11*, 2459–2469.
- [27] P. Simon, *ACS Nano* **2017**, *11*, 2393–2396.
- [28] C. Yang, Y. Liu, X. Sun, Y. Zhang, L. Hou, Q. Zhang, C. Yuan, *Electrochim. Acta* **2018**, *271*, 165–172.
- [29] M. R. Lukatskaya, S.-M. Bak, X. Yu, X.-Q. Yang, M. W. Barsoum, Y. Gogotsi, *Adv. Energy Mater.* **2015**, *5*, 1500589.
- [30] A. C. Ferrari, J. Robertson, *Phys. Rev. B* **2000**, *61*, 14095–14107.
- [31] A. C. Ferrari, *Solid State Commun.* **2007**, *143*, 47–57.
- [32] A. C. Ferrari, J. Robertson, *Phys. Rev. B* **2001**, *64*, 075414.
- [33] H. Lindström, S. Södergren, A. Solbrand, H. Rensmo, J. Hjelm, A. Hagfeldt, S.-E. Lindquist, *J. Phys. Chem. B* **1997**, *101*, 7717–7722.
- [34] Q. Jiang, N. Kurra, M. Alhabeb, Y. Gogotsi, H. N. Alshareef, *Adv. Energy Mater.* **2018**, *8*, 1703043.

Manuscript received: September 10, 2019

Accepted manuscript online: October 1, 2019

Version of record online: October 22, 2019